

Elastic scattering signals of solar neutrinos with enhanced baryonic currents

Maxim Pospelov^(a,b) and Josef Pradler^(a)

^(a)*Perimeter Institute for Theoretical Physics, Waterloo, ON, N2L 2Y5, Canada*

^(b)*Department of Physics and Astronomy, University of Victoria,
Victoria, BC, V8P 1A1 Canada*

Abstract

The coupling of the baryonic current to new neutrino states ν_b with strength in excess of the weak interactions is a viable extension of the Standard Model. We analyze the signature of ν_b appearance in the solar neutrino flux that gives rise to an elastic scattering signal in dark matter direct detection and in solar neutrino experiments. This paper lays out an in-depth study of ν_b detection prospects for current and future underground rare event searches. We scrutinize the model as a possible explanation for the reported anomalies from DAMA, CoGeNT, and CRESST-II and confront it with constraints from other null experiments.

1 Introduction

The phenomenon of neutrino mass-mixing and thereby induced lepton-flavor oscillations constitute the only conclusively detected deviation from the Standard Model (SM) to date. Though the neutrino sector is certainly the most elusive part of the SM, a tremendous and sometimes painstaking experimental effort has firmly established the patterns of mass splitting and mixing for the three SM neutrinos, ν_e , ν_μ , ν_τ . The multitude of data is consistent with neutrino flavor eigenstates being the linear combination of—at least—three massive ones ν_1 , ν_2 , ν_3 , with mass-squared differences $\Delta m_{21}^2 = \mathcal{O}(10^{-5}) \text{ eV}^2$ and $\Delta m_{31}^2 \sim \Delta m_{32}^2 = \pm \mathcal{O}(10^{-3}) \text{ eV}^2$ and mixing angles with magnitudes $\sin^2 2\theta_{13} \sim 0.1$, $\theta_{23} \sim \pi/4$, $\tan^2 \theta_{12} \sim 1/2$ [1, 2]. Neutrinos are predominantly detected via their charged current (CC) interaction on matter, and elastic scattering (ES) on electrons. The only pure neutral current (NC) process for solar neutrinos with participation of all active neutrino flavors observed remains the deuteron breakup reaction $d + \nu_x \rightarrow p + n + \nu_x$ in the SNO experiment [3, 4].

On the theoretical side, the interest to the elastic scattering of neutrinos on nuclei dates back to Drukier and Stodolsky [5], who outlined their vision of a true neutrino observatory: neutrinos with MeV-scale energies as they emerge from the interior of the sun, from nuclear reactors, from spallation beam experiments, or from supernovae explosions can scatter elastically and with N^2 enhancement in the cross section on keV-scale recoiling nuclei of N neutrons [6]. Even though the energy transfer to the target nucleus is small, the idea was that its effect in a detector at cryogenic temperatures may be macroscopic given that the specific heat of the material can be minute. The underlying principle of NC neutrino scattering on nuclei has found its proliferation in Dark Matter (DM) searches for weakly interacting massive particles (WIMPs) [7].

Direct detection experiments seek for evidence of DM via its elastic scattering on various targets such as crystals made from germanium or liquefied noble gases such as xenon. No univocal evidence for DM has yet been found but upper limits as low as $7 \times 10^{-45} \text{ cm}^2$ [8] in the WIMP-nucleon cross section have been inferred for the optimal range of recoil energies. These experiments have reached a level in sensitivity such that neutrino coherent scattering on nuclei is being discussed as potential background for future ton-scale experiments; see *e.g.* [9, 10]. The latter process has a cross section $\sigma_\nu/N^2 \simeq 4 \times 10^{-43} (E_\nu/10 \text{ MeV})^2 \text{ cm}^2$ where E_ν is the neutrino energy. Indeed, the average flux of neutrinos at earth, dominated by the solar pp -chain of thermonuclear reactions, $\Phi_\nu^{pp} \simeq 6 \times 10^{10} \text{ cm}^{-2} \text{ s}^{-1}$ [11], exceeds the flux expected from WIMPs, $\Phi_{\text{DM}} \sim 10^5 (100 \text{ GeV}/m_{\text{DM}}) \text{ cm}^{-2} \text{ s}^{-1}$, by many orders of magnitude. The reason why neutrinos are *not* copiously detected via their NC interaction in DM experiments lies in the soft recoil spectrum they induce, $E_R \leq 2E_\nu^2/m_N \simeq 2 \text{ keV} \times (100/A) (E_\nu/10 \text{ MeV})^2$, where m_N and A are the mass and atomic mass number of the target nucleus. Whereas these experiments fall short in sensitivity to SM neutrinos, they may nonetheless be powerful probes of an extended neutrino sector [12].

This paper surveys potential signatures of the existence of yet another “sterile-active” neutrino state, ν_b , where active is understood in the sense that ν_b shall interact via a *new* neutral current interaction with baryons (NCB) [12]. This “baryonic” neutrino is also “sterile” in that it shares no SM NC or CC interactions. In particular, this implies that ν_b does not scatter elastically on electrons. Remarkably, ν_b can then be coupled to baryons with a

strength G_B which exceeds that of the weak interactions substantially, $G_B/G_F = (10^2 - 10^3)$; G_F is the Fermi constant. This, in turn, implies the existence of a force mediator with the mass much smaller than m_W . The key observation made in [12] is that for MeV-scale energies of ν_b the ratio of elastic to inelastic cross section with nuclei scales as

$$\frac{\sigma_{\nu_b N}(\text{elastic})}{\sigma_{\nu_b N}(\text{inelastic})} \sim 10^8 \times \left(\frac{A}{100}\right)^2 \left(\frac{10 \text{ MeV}}{E_\nu}\right)^4 \left(\frac{2 \text{ fm}}{R_N}\right)^4, \quad (1)$$

where R_N denotes a nuclear radius. This tremendous enhancement opens an exciting phenomenological window of opportunity: ν_b states can be searched for in the growing number of direct detection dark matter experiments. The less constrained choice of parameters for this model is when the oscillation length for $\nu_{SM} \rightarrow \nu_b$ transition is long enough not to create any significant fluxes of reactor/beam/atmospheric neutrinos, while for solar neutrinos one can have a sizable fraction of ν_b . In particular, solar ^8B neutrinos have the best combination of large flux and high end-point energy for producing an observable signal in rare event searches. Relation (1) makes even small scale DM searches competitive with dedicated large target-mass neutrino experiments in their sensitivity to ν_b that originate from ^8B neutrinos.

Moreover, as proposed in [12], if the oscillation length of ν_b is on the order of the earth-sun distance, the signal may be annually modulated in a non-trivial way, with a possibility of a bigger flux in the summer, and with modulation amplitude larger than naively expected. In this paper we analyze this corner of the parameter space in great detail, as it could offer a ν_b -scattering explanation to the DAMA signal [13, 14] while still being compatible with other null-results from DM experiments; for a relevant collider study in this context cf. [15]. The long-standing DAMA “anomaly” has very recently received some additional impetus by the reports [16, 17] of the CoGeNT collaboration on 1) an unexpected rise in observed events at low nuclear recoils and 2) an indication of annual modulation, see *e.g.* [17, 18, 19, 20]. Finally, the CRESST-II experiment has published results of its latest run, which had some population of unexpected events on top of existing backgrounds [21].

The attempts to explain positive signals (DAMA) and possible hints on non-zero signals (CoGeNT, CRESST) while staying consistent with null results of other groups, are widespread in the WIMP literature, see *e.g.* [22, 23, 24, 25, 26, 27, 28, 29, 30] and references therein. The models that fare best feature ~ 10 GeV WIMP masses, although the overall consistency of the “light WIMP” explanation for the “DM anomalies” remains doubtful. In this paper, we provide an in-depth critical assessment of ν_b models with regard to their potential to explain positive signals, and make predictions for the upcoming experiments, paying attention to those that could potentially differentiate between ν_b and light dark matter recoils. We leave other phenomenological aspects of this interesting, but to date a relatively poorly explored model to subsequent work.

This paper is organized as follows: in the next section, the baryonic neutrino model is reviewed. In Sec. 3 we cover the current and future sensitivity of DM searches to ν_b and study the potential explanation of the DAMA, CoGeNT, and CRESST-II signals. In Sec. 4 the elastic scattering of ν_b in neutrino experiments is considered, and in Sec. 5 we reach our conclusions.

2 Baryonic neutrinos

In the baryonic neutrino model [12], the SM gauge group is extended by an abelian factor $U(1)_B$. The new neutrino is a left-chiral field $\nu_b = \frac{1}{2}(1 - \gamma^5)\nu_b$ with charge $q_b = \pm 1$ and gauge coupling $g_l > 0$. Leptons are neutral under $U(1)_B$ but all quarks $q = Q_L, u_R, d_R$ carry baryonic charge $1/3$ with gauge coupling $g_b > 0$. The SM Lagrangian is supplemented by the following terms

$$\mathcal{L}_B = \bar{\nu}_b \gamma^\mu (i\partial_\mu - g_l q_b V_\mu) \nu_b - \frac{1}{3} g_b \sum_q \bar{q} \gamma^\mu q V_\mu - \frac{1}{4} V_{\mu\nu} V^{\mu\nu} + \frac{1}{2} m_V^2 V_\mu V^\mu + \mathcal{L}_m. \quad (2)$$

We have assumed that the new gauge field V_μ with field strength $V_{\mu\nu}$ has acquired a mass m_V by the spontaneous breakdown of the $U(1)_B$ symmetry with Higgs_b VEV $\langle \phi_b \rangle = v_b/\sqrt{2}$; the sum in the second term runs over all SM quarks q . The part \mathcal{L}_m is responsible for generating neutrino masses and the mixing between SM neutrinos and the new state ν_b . A simple UV-completion of \mathcal{L}_m is one where—once electroweak symmetry and $U(1)_b$ are broken—new right-handed neutrinos ν_R induce mass terms for SM neutrinos as well as for ν_b :

$$\mathcal{L}_m = \frac{1}{2} N_L^T \mathcal{C}^\dagger M N_L + \text{h.c.}, \quad N_L = \begin{pmatrix} \nu'_L \\ \nu'^C_R \\ \nu'_b \end{pmatrix}, \quad M = \begin{pmatrix} 0 & m_D^T & 0 \\ m_D & m_R & v_b b \\ 0 & v_b b^T & 0 \end{pmatrix}. \quad (3)$$

Here, ν'_L denote the three SM neutrinos with Dirac mass matrix m_D , $\nu'^C_R = \mathcal{C} \overline{\nu'_R}^T$ are the charge conjugate states of ν'_R with Majorana mass matrix m_R , and b is a vector of Yukawa couplings generating mass for ν'_b . In the simplest case the new right-handed neutrinos generate masses for ν'_L and ν'_b simultaneously. Introduction of a right-handed partner for ν'_b will cancel a $U(1)_B^3$ triangle anomaly and remaining gauge anomalies can be cured by the introduction of a new family of heavy fermions with appropriate quantum numbers [31]. From the phenomenological viewpoint the details of this will not be of importance for this work.

The mass matrix M in (3) is diagonalized by $\mathcal{M}_{\text{diag}} = (V_L^\nu)^\dagger M V_L^\nu$ where V_L^ν is a unitary matrix, defining the mass eigenstates $N_L = (V_L^\nu)^\dagger N'_L$. Diagonalization of the charged lepton mass matrix by 3×3 unitary matrices $V_{L,R}^l$ with mass eigenstates $l_L = (V_L^l)^\dagger l'_L$, and $l_R = (V_R^l)^\dagger l'_R$ where $l = (e^-, \mu^-, \tau^-)$ then determines the mixing among the SM active neutrino states. Assuming that the eigenvalues of m_R are much larger than any other values in M , the seesaw mechanism is operative and one can integrate out the heavy, right handed states. We are left with the 4×4 mixing matrix U which connects “flavor” $\nu_{\alpha L}$ ($\alpha = e, \mu, \tau, b$) and mass n_{kL} ($k = 1, \dots, 4$) eigenstates:

$$n_{kL} = \sum_\alpha U_{k\alpha}^* \nu_{\alpha L}, \quad U = \begin{matrix} & \begin{matrix} 1 & 2 & 3 & 4 \end{matrix} \\ \begin{matrix} e \\ \mu \\ \tau \\ b \end{matrix} & \begin{pmatrix} & & & \cdot \\ U_{\text{PMNS}} & & & \cdot \\ & & & \cdot \\ \cdot & \cdot & \cdot & \cdot \end{pmatrix} \end{matrix}, \quad (4)$$

where U_{PMNS} is the usual 3×3 mixing matrix among the active flavors [1]. The NCB current in the respective interaction and mass eigenbasis reads

$$j_{NCB}^\mu = \bar{\nu}_b \gamma^\mu \nu_b = \sum_{k,k'} U_{4k}^* U_{4k'} \bar{n}_{kL} \gamma^\mu n_{k'L}. \quad (5)$$

2.1 Neutrino oscillations and matter effects

Aiming at a scenario in which the baryonic neutrino is coupled stronger than G_F , the question which immediately arises is whether new matter effects are to play a role. The index of refraction of ν_b -propagation in matter is found by computing the forward scattering amplitude of ν_b on matter, described by the effective Lagrangian

$$\mathcal{L}_{\text{eff}} = -G_B j_{NCB}^\mu \sum_{N=n,p} \bar{N} \gamma_\mu N, \quad G_B = q_b \frac{g_b g_l}{m_V^2} = q_b \mathcal{N} G_F. \quad (6)$$

In the last equality we have introduced the parameter $\mathcal{N} > 0$ to measure G_B in units of G_F with the sign of the interaction determined by the charge q_b of ν_b . In an unpolarized medium, one obtains the following matter potential

$$V_{NCB} = \pm q_b \mathcal{N} G_F n_B (Y_N + 2Y_{\nu_b}), \quad Y_f = \frac{n_f - n_{\bar{f}}}{n_B}, \quad (7)$$

where the plus sign is for ν_b and the minus sign for $\bar{\nu}_b$; Y_f is the particle-antiparticle asymmetry, normalized to the number density of baryons n_B . The first term in the first equation describes the potential in ordinary matter while the second term is the potential for $\nu_{bL}^{(-)}$ in a hypothetical sea of baryonic neutrinos.

In ordinary matter, with mass fraction X_p in form of bound or unbound protons, the induced matter potentials (up to coherence factors) compare as follows

$$V_{NCB} : V_{CC} : V_{NC} = q_b \mathcal{N} : \sqrt{2} X_p : -\sqrt{2} (1 - X_p) / 2, \quad (8)$$

where we have made use of the charge neutrality condition. As is evident, for $\mathcal{N} \gg 1$ baryonic neutrinos experience the largest matter effect since X_p is always of order unity.

The large strength of the NCB interaction may suggest that the flavor evolution in matter is dominated by V_{NCB} . In a simplified two-neutrino case the Schrödinger-like equation describing the transition probabilities $P_{\alpha \rightarrow \beta}(x) = |\langle \nu_\beta | \nu_\alpha(x) \rangle|^2 \equiv |\psi_{\alpha\beta}(x)|^2$ from an initial state $|\nu_\alpha(0)\rangle$ to final state $|\nu_\beta\rangle$ can then be brought into the following form

$$i \frac{d}{dx} \begin{pmatrix} \psi_{\alpha\alpha} \\ \psi_{\alpha b} \end{pmatrix} \simeq \frac{1}{4E_\nu} \begin{pmatrix} -\Delta m^2 \cos 2\theta - 2E_\nu V_{NCB} & \Delta m^2 \sin 2\theta \\ \Delta m^2 \sin 2\theta & \Delta m^2 \cos 2\theta + 2E_\nu V_{NCB} \end{pmatrix} \begin{pmatrix} \psi_{\alpha\alpha} \\ \psi_{\alpha b} \end{pmatrix}. \quad (9)$$

Here, E_ν is the neutrino energy and $\theta = \theta_{k4}$ and $\Delta m^2 = \Delta m_{4k}^2$ with $k = 1, 2, 3$ for $\alpha = e, \mu, \tau$ are the vacuum mixing angle and the mass squared difference between the new massive state ν_4 and SM neutrinos $\nu_{1,2,3}$, respectively. The matter induced mixing angle θ_M reads

$$\tan 2\theta_M = \frac{\tan 2\theta}{1 + 2E_\nu V_{NCB} / (\Delta m^2 \cos 2\theta)}, \quad (10)$$

and, since $\text{sign}(V_{NCB}) = q_b$, resonant flavor transitions for ν_b could be possible for $q_b = +1$ and $\theta > \pi/4$ or for $q_b = -1$ and $\theta < \pi/4$ (and vice versa for $\bar{\nu}_b$.) We note, however, that the efficiency of a transition has a separate dependence on Δm^2 , unrelated to Eq. (10), as the matter-induced oscillations cease to occur in the limit of $\Delta m^2 \rightarrow 0$. From (10) we find the necessary condition for which NCB effects are least likely to play a role,

$$\Delta m^2 \cos 2\theta \ll 10^{-4} \text{ eV}^2 \times \left(\frac{E}{10 \text{ MeV}} \right) \left(\frac{\mathcal{N}}{100} \right) \left(\frac{\rho}{\text{g/cm}^3} \right). \quad (11)$$

In this work we focus on a parameter region which obeys this limit. A discussion for larger values of Δm^2 is beyond the scope of this work.

2.2 Solar ν_b flux

Let us consider a scenario in which the baseline of ν_b oscillation L_{osc} is on the order of the earth-sun distance, $L_0 = 1 \text{ AU} \simeq 1.5 \times 10^8 \text{ km}$. This “just-so” choice of parameters suggests a canonical mass squared difference,

$$\frac{L_{\text{osc}}}{L_0} \simeq 0.5 \times \left(\frac{10^{-10} \text{ eV}^2}{\Delta m^2} \right) \left(\frac{E_\nu}{10 \text{ MeV}} \right). \quad (12)$$

“Flavor” eigenstates $\nu_{\alpha L}$ ($\alpha = e, \mu, \tau, b$) are found from mass-eigenstates n_{kL} by inversion of (4), $\nu_{\alpha L} = \sum_k U_{\alpha k} n_{kL}$, and their evolution is obtained by solving

$$i \frac{d\Psi}{dx} = \mathcal{H} \Psi, \quad \mathcal{H} = \frac{1}{2E} (U \mathcal{M}_d^2 U^\dagger + \mathcal{A}). \quad (13)$$

Here Ψ is the vector of amplitudes for the flavor states, $\Psi = (\psi_e, \psi_\mu, \psi_\tau, \psi_b)$, $\mathcal{M}_d^2 = \text{diag}(m_1^2, m_2^2, m_3^2, m_4^2)$ is the diagonalized mass matrix and the entries of $\mathcal{A} = \text{diag}(A_{CC} + A_{NC}, A_{NC}, A_{NC}, A_{NCB})$ are related to the induced matter potentials via $A_x = 2EV_x$. In general, the baryonic neutrino flux at the Earth location is found upon numerical integration of (13) from the production point r_0 of ν_e in the solar interior to earth at distance L with initial condition $\Psi(r_0) = (1, 0, 0, 0)$. This could be a complex problem when matter effects are involved, but fortunately not for the region of the parameter space we are interested in.

With a few simplifying assumptions the appearance probability at earth can be obtained analytically [12]. We seek access to the high energy end of the neutrino spectrum, $E_\nu \gtrsim 10 \text{ MeV}$, because scatterings of ν_b will then more likely be picked up by a detector. The largest flux in combination with high endpoint energy comes from the neutrino emission in the decay of ${}^8\text{B}$. With ${}^4\text{He}$ being the most tightly bound light nucleus, hep neutrinos have the highest endpoint in energy but come with a flux which is smaller by three orders of magnitude. The ${}^8\text{B}$ and hep respective fluxes and endpoint energies are given by [32],

$$\begin{aligned} \Phi_{8\text{B}} &= (5.69^{+0.173}_{-0.147}) \times 10^6 \text{ cm}^{-2} \text{ s}^{-1}, & E_{\text{max}, 8\text{B}} &= 16.36 \text{ MeV}, \\ \Phi_{\text{hep}} &= (7.93 \pm 0.155) \times 10^3 \text{ cm}^{-2} \text{ s}^{-1}, & E_{\text{max}, \text{hep}} &= 1.88 \text{ MeV}. \end{aligned} \quad (14)$$

In the solution to the solar neutrino problem the MSW effect dominates the flavor evolution of the highly energetic part of the neutrino spectrum and neutrinos exit the sun mainly as ν_2 .

Therefore, we assume a preferential mixing of the new neutrino to ν_2 , $\theta_{24} \neq 0$, and neglect other mixings of ν_4 to the active states. Choosing $q_b > 0$, no resonant flavor transitions to ν_b inside the sun appear and with a ballpark of Δm^2 suggested in (12) the standard solar MSW solution remains in place.

With these assumptions and using a tri-bimaximal mixing ansatz for the active states the following ν_b appearance probability at earth for the high energy part of the ^8B (and hep) fluxes has been obtained in [12],

$$P_{eb}(L, E_\nu) \simeq \sin^2(2\theta_b) \sin^2 \left[\frac{\Delta m_b^2 L(t)}{4E_\nu} \right]. \quad (15)$$

It is assumed that mass mixings among active components are larger than mixings with ν_b so that one can address the diagonalization of the neutrino mass matrix sequentially. In this procedure, Δm_b^2 and θ_b denote the associated effective mass-squared difference and mixing angle between ν_2 and ν_b , respectively. The true vacuum mass eigenstates are $\nu_I = \cos \theta_b \nu_2 + \sin \theta_b \nu_b$ and $\nu_{II} = -\sin \theta_b \nu_2 + \cos \theta_b \nu_b$ and a phase builds up between ν_2 exit from the sun and propagation to the detector at distance L ,

$$L(t) = L_0 \left\{ 1 - \epsilon \cos \left[\frac{2\pi(t - t_0)}{T} \right] \right\}, \quad (16)$$

where $\epsilon = 0.0167$ is the ellipticity of the earth's orbit; the perihelion is reached at $t_0 \sim 3$ Jan. In what follows, it will be convenient to introduce an effective interaction parameter \mathcal{N}_{eff} ,

$$\mathcal{N}_{\text{eff}}^2 = \mathcal{N}^2 \sin^2(2\theta_b)/2. \quad (17)$$

In the limit of rapid oscillations this implies $P_{eb} G_B^2 \rightarrow \mathcal{N}_{\text{eff}}^2 G_F^2$.

3 Direct Detection

In this section we provide a detailed investigation of current and future direct detection experiments. From the scaling (1) we expect that elastic scattering off nuclei in direct detection experiments constitutes one of the most promising avenues in the search for a solar, long-baseline flux of ν_b particles.

The spin-independent elastic recoil cross section on nuclei obtained from (6) essentially resembles the one from neutrino-nucleus coherent scattering [5] with the replacement $G_F^2 (N/2)^2 \rightarrow G_B^2 A^2$ [12],

$$\frac{d\sigma_{\text{el}}}{d\cos\theta_*} = \frac{G_B^2}{4\pi} E_\nu^2 A^2 (1 + \cos\theta_*). \quad (18)$$

Here A is the atomic number of the nucleus and θ_* is the scattering angle in the CM frame. Equation (18) can be rewritten in terms of a recoil cross section,

$$\frac{d\sigma_{\text{el}}}{dE_R} = \frac{G_B^2}{2\pi} A^2 m_N F^2(|\mathbf{q}|) \left[1 - \frac{(E_{\text{min}})^2}{E_\nu^2} \right], \quad E_R = \frac{E_\nu^2}{m_N} (1 - \cos\theta_*), \quad (19)$$

where $E_{\min} = \sqrt{E_R m_N/2}$ is the minimum energy required to produce a recoiling nucleus of mass m_N and kinetic energy E_R . Here we have now included the nuclear form factor suppression $F^2(|\mathbf{q}|)$ for scatterings with three-momentum transfer \mathbf{q} , and in our numerical evaluations we use the Helm form factor parametrization [33] with the nuclear skin thickness of 0.9 fm.

For the sake of comparison to the simplest case of spin-independent scattering of DM on nuclei, we can evaluate the total elastic scattering cross section of ν_b on nuclei (at zero momentum transfer),

$$\sigma_{\text{el}} = \frac{G_B^2}{\pi} A^2 E_\nu^2 \simeq 1.7 \times 10^{-38} \text{ cm}^2 \times A^2 \left(\frac{\mathcal{N}}{100} \right)^2 \left(\frac{E_\nu}{10 \text{ MeV}} \right)^2. \quad (20)$$

The coefficient in front of the second relation serves as a figure of merit when compared to the DM-nucleon cross section σ_n . Given that direct detection experiments have put upper limits on σ_n as low as 10^{-44} cm^2 [8] the coefficient in (20) is sizable. However, a much more stringent cut off in E_R makes it increasingly difficult for an essentially massless ν_b to scatter off heavier targets.

The recoil spectrum arising from the solar flux of ν_b will have to include an average over the neutrino energy spectrum df_i/dE_ν of neutrino source i , weighted by the ν_b appearance probability and an overall flux modulation $[L_0/L(t)]^2$ due to the earth's eccentric orbit,

$$\frac{dR}{dE_R} = N_T \left[\frac{L_0}{L(t)} \right]^2 \sum_i \Phi_i \int_{E_{\min}}^{E_{\max,i}} dE_\nu P_{eb}(t, E_\nu) \frac{df_i}{dE_\nu} \frac{d\sigma_{\text{el}}}{dE_R}. \quad (21)$$

Note that P_{eb} depends on E_ν so that it has to be included into the average; Φ_i is the integral flux given in (14) and df_i/dE is normalized to unity, $\int dE df_i/dE = 1$, and taken from [34, 35]. N_T denotes the number of target nuclei per unit detector mass, and in our computations we take the fractional isotopic abundances of each element under consideration into account. The rate exhibits a non-trivial time-dependence. The maximum of the overall flux is attained at the perihelion in early January. However, the integral in Eq. (21) constitutes an additional source of modulation which depends on the neutrino energy. It will have its strongest effect on the differential rate in the "just-so" regime of Eq. (12) where L_{osc} is on the order of the sun earth distance; we exploit this fact in the following section.

The left panel of Fig. 1 shows the solar neutrino spectra of the various sources. In the right panel we compute the associated recoil spectra using (21) for a germanium detector without threshold, with perfect energy resolution, and an exposure of $1 \text{ kg} \times \text{yr}$. For simplicity and since it does not affect the argument we use P_{eb} as given in (15) for all fluxes, while strictly speaking Eq. (15) is only valid in the MSW regime. The deviation from MSW only affects the softest recoils, and can therefore be safely neglected in what follows. As can be seen, only ^8B and hep neutrinos reach out to values of $E_R \gtrsim \text{few keV}$ where direct detection experiments become sensitive. Furthermore, ^8B neutrinos constitute the dominant part of the signal with hep giving a small correction only.

The spectrum in (21) is a theoretical one. To make contact with experiment we include effects from energy resolution, detector threshold and quenching of nuclear recoil energy. Details will be given when discussing the respective experiments. We start our discussion by considering the experiments with putative positive signal claims.

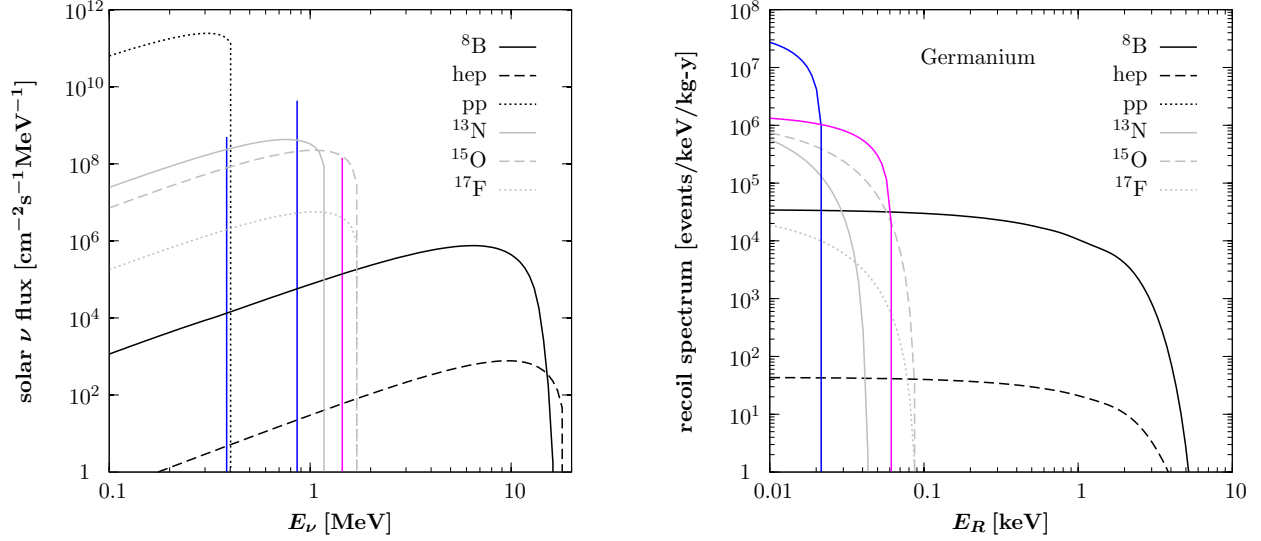


Figure 1: *Left:* Solar neutrino fluxes as a function of energy as taken from [34, 35, 36]. *Right:* Associated recoil spectrum in a (perfect) germanium detector with a total exposure of 1 kg \times yr. Only ^8B and hep neutrinos reach out to values of E_R where direct detection experiments become sensitive.

3.1 DAMA

The DAMA/NaI and its upgrade the DAMA/LIBRA experiment [37], situated in the northern hemisphere at the underground Gran Sasso National Laboratory (LNGS), were the first to report on a potential direct DM detection. The experiment uses large radiopure NaI(Tl) crystals to measure scintillation light resulting from nuclear recoils. Given that there is no other discriminating channel except requiring the candidate event to be a “single-hit”, a relatively large overall count-rate of ~ 1 cpd/kg/keVee is observed. The presence of a positive signal is inferred from the annual modulation of the residual count rate on the order of ~ 0.02 cpd/kg/keVee over low-energy bins between 2 and 6 keVee once the average count rate per cycle is subtracted [13, 14]; for recent discussions on potential modulating backgrounds see [38, 39, 40, 41, 42].

The modulation of the event rate has been observed over the course of more than a dozen annual cycles, collecting a cumulative exposure of 1.17 ton \times yr [13, 14]. The null-hypothesis, *i.e.* a rate constant in time, has been excluded at the 8.9σ level. The residuals of the DAMA/LIBRA runs in consecutive bins between (2-4) keV, (2-5) keV and (2-6) keV are shown by the data points in Fig. 3. The DAMA signal is usually decomposed as

$$S = S_0 + S_m \cos[\omega(t - t_0)] \quad (22)$$

where $S_0 \sim 1$ cpd/kg/keVee is the baseline rate of single hit events and S_m is the modulation amplitude,

$$S_m = \frac{1}{2} \left(\left. \frac{dR}{dE_\nu} \right|_{t_0} - \left. \frac{dR}{dE_\nu} \right|_{t_0+1/2 \text{ yr}} \right). \quad (23)$$

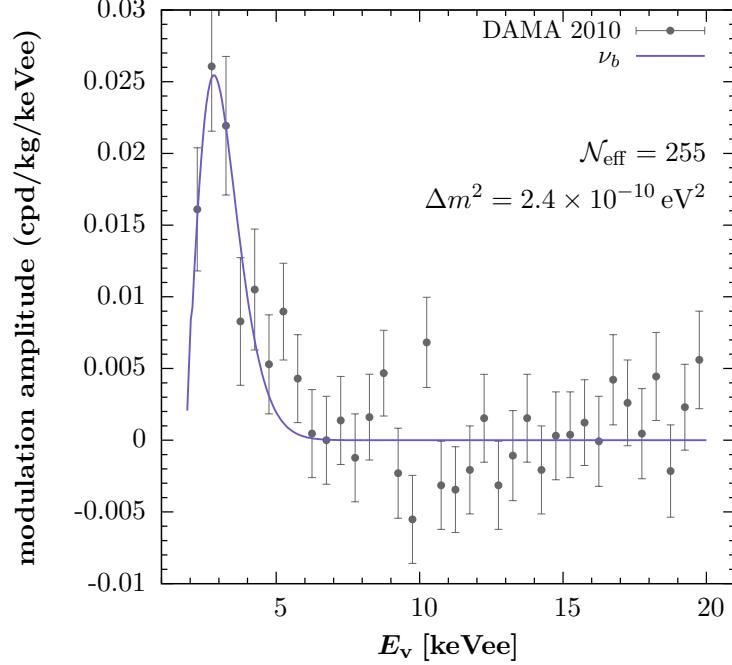


Figure 2: The data points show the DAMA modulation amplitude as reported in [14] in units of counts per day (cpd) per kg detector material and recoil energy. The solid line is the best fit from ν_b to the data.

The measured phase t_0 is reported to be compatible with the one expected from DM, $t_0 = 152.5$ days (June 2nd) with a period of one year, *i.e.* $\omega = 2\pi/(1 \text{ yr})$. The reported modulation amplitude is shown by the data points in Fig. 2.

To see if ν_b provides a viable explanation of the DAMA data one can either fit the modulation spectrum (23) or directly the time series of the residual rate. Considering the solar ν_b origin for DAMA, Eq. (21) may not necessarily lead to a truly sinusoidal form of the signal as a function of time. In addition, t_0 is not expected to be identical with the DM value of 152.5 days. At first sight, a direct fit of the time series seems therefore favorable. However, the reported residuals are binned in energy so that they only provide coarse-grained information on the recoil energy distribution. This, in contrast, calls for a fit of the modulation amplitude instead. We have implemented both approaches and discuss their results below. In addition, one can also attempt a joint fit of both data sets. This approach is complicated by the fact that the data sets are not independent.

We start by fitting the modulation amplitude. Observable scatterings of ν_b occur on sodium only and no appreciable rate is expected for $E_v \gtrsim 7 \text{ keVee}$. The latter expectation is in accordance with what is seen in the data. Therefore, we only fit the first ten data points with $E_v \lesssim 7 \text{ keVee}$ in order not to bias the goodness-of-the-fit estimate. With the help of the usual χ^2 function we obtain the following best fit values,

$$\text{DAMA } S_m : \quad \Delta m_b^2 = 2.43 \times 10^{-10} \text{ eV}^2, \quad \mathcal{N}_{\text{eff}} = 255, \quad \chi_{\text{min}}^2/n_d = 9.5/8. \quad (24)$$

The minimum in χ^2 is associated with a p -value of $p = 0.3$; n_d denotes the number of degrees of freedom. The result of this fit is shown by the solid line in Fig. 2. Confidence regions in

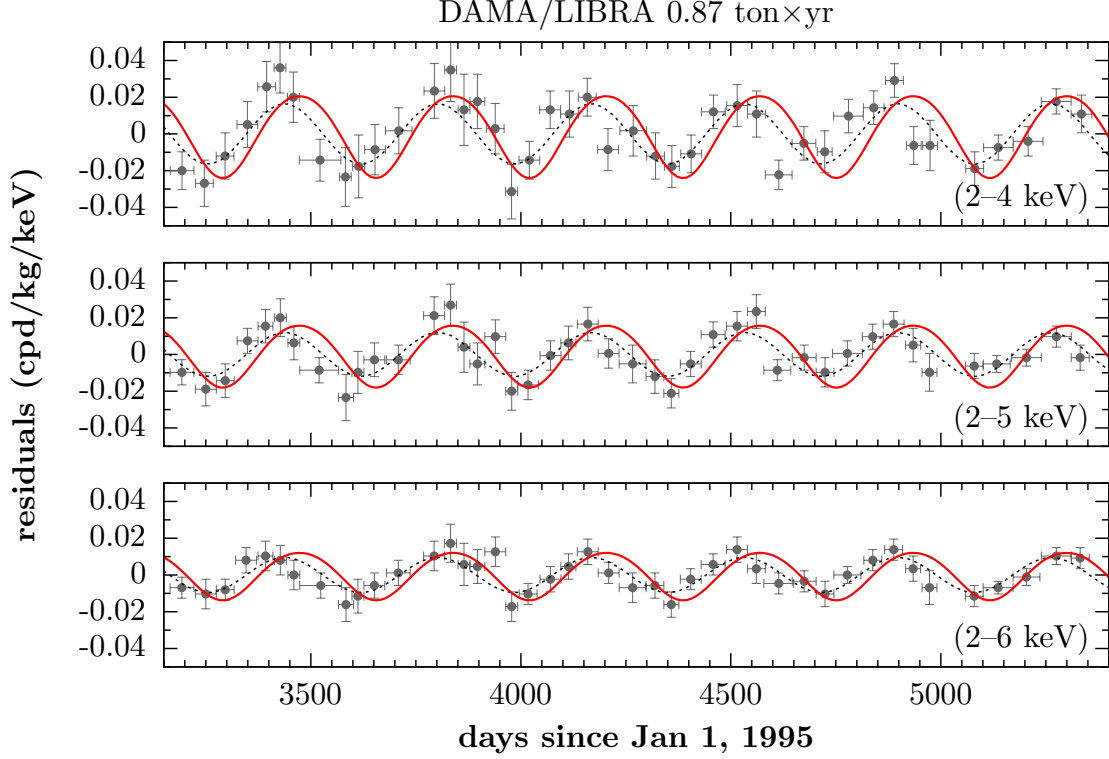


Figure 3: The data points show the DAMA/LIBRA reported residual event rate for various energy bins as a function of time. The red line is the residual event rate associated with the fit to the modulation amplitude in Fig. 2. The dotted line is a fit of the sinusoidal function $A \times \cos[\omega(t - t_0)]$ with ω corresponding to a period of one year and a phase t_0 as expected from DM. As can be seen the ν_b signal is approximately out of phase by one month. For a quantitative statement see main text.

Δm_b^2 and \mathcal{N}_{eff} are constructed by demanding,

$$\chi^2(\Delta m_b^2, \mathcal{N}_{\text{eff}}) \leq \chi_{\text{min}}^2 + \Delta\chi^2, \quad (25)$$

where χ_{min}^2 is given in (24). We choose $\Delta\chi^2 = 9.21$ which corresponds to generous 99% C.L. regions. The choice results in the two disjoint gray shaded regions shown in Fig. 6.

The above result looks promising. However, in contrast to the DM case one has to check how well the time dependence of the rate is met. The resulting signals in the various energy bins from the best fit values (24) are shown by the solid (red) lines in Fig. 3. For completeness we also show by the dotted lines fits of the data by the sinusoidal function $A_i \cos[\omega(t - t_0)]$ with period 1 yr and $t_0 = \text{June 2}^{\text{nd}}$ as expected when the origin were due to DM scatterings. As can be seen by eye, the ν_b signals seems to lag behind by approximately one month. Thus, the best fit corresponds to a phase inversion with a maximum rate at the aphelion with $t_0 \sim \text{July 5th}$. For example, using the (2 – 4) keV residuals, the best fit values of the modulation spectrum (24), one finds $\chi^2/n_d = 101/41$ with $p = 5 \times 10^{-7}$ for the residuals. This points towards a very poor description of the full data.

We can try to improve on the above situation by directly fitting the residual rate. This is an important check, since the time dependence of Eq. (21) is non-trivial. Can we find a

corner in the considered parameter space in which one can alleviate the tension in the phase of DAMA and the ν_b signal? From the $(2 - 4)$ keVee data we obtain as best fit,

$$\text{DAMA residuals: } \Delta m_b^2 = 2.45 \times 10^{-10} \text{ eV}^2, \quad \mathcal{N}_{\text{eff}} = 183, \quad \chi_{\text{min}}^2/n_d = 73.2/41. \quad (26)$$

Though the fit fares slightly better on the residuals with $p \simeq 10^{-3}$, this does not ameliorate the situation sufficiently. Moreover, the smaller value of \mathcal{N}_{eff} now somewhat under-predicts the modulation amplitude. Finally, even when we perform a joint fit (neglecting potential covariances of the data sets) we do not find any substantial improvement. We conclude, that even though the DAMA modulation amplitude is fit rather nicely, the time series of events speaks against the ν_b interpretation.

As a final remark, we comment on the sodium quenching factor. For our analysis above we used $Q = 0.3$ in the conversion to electron equivalent recoil energy, $E_v(\text{keVee}) = QE_R(\text{keV})$. New measurements [43] seem to indicate 1) lower values $Q \sim 0.15$ and 2) a stronger energy dependence as previously thought. This has important implications for light DM as well as for the ν_b hypothesis. We find that $Q = 0.15$ moves the DAMA regions in Fig. 6 towards larger values of \mathcal{N}_{eff} which are already excluded by all the other considered null searches. The situation then becomes more similar to the one already witnessed for DM.

3.2 CoGeNT

The CoGeNT experiment is a low-threshold nuclear recoil germanium detector situated in the Soudan Underground Laboratory. The latest data release is based on 442 live days taken with 0.33 kg target [16, 17]. An unexplained exponential rise of the signal at lowest recoil energies 0.5–1 keVee is observed. The origin of it is unknown and has lead to the speculation that DM with a mass in the $\sim 8 - 10$ GeV range may be the cause of it. For spin-independent DM-nucleus scattering, the excess requires a cross section $\sigma_{SI} \sim 10^{-40} \text{ cm}^2$. Such values are challenged by the null-result of XENON100 and by the low-threshold analysis of CDMS-II. However, more recently the collaboration has identified a source of surface-background events which may lead to a revision of the signal strength in the low-recoil bin 0.5–1 keVee. In the following we will investigate the possibility that the observed excess may be due to scattering of ν_b in the detector. We will also account for the possibility that the collaboration's results could be revised in the near future [43].

In addition to the signal-rise below 1 keVee the data also appears to be annually modulated in the 0.5–3.2 keVee bracket. The observed event rate peaks in mid-to-late April (2010) with a modulation amplitude of $\sim 16\%$, most pronounced between 1.4–3.2 keVee [17]. The latter behavior is neither expected from DM scatterings nor could it be explained by ν_b scatterings since the recoil spectrum arising from ^8B neutrinos is cut off for $E_v \gtrsim 1.4$ keVee. We also note that the modulation of nuclear recoil events in Ge in that energy regime has recently been challenged in a dedicated analysis by CDMS [44]. We will therefore not further address the potential modulation of the CoGeNT signal and await further data.

Cosmogenically induced radioactive background has to be subtracted from the CoGeNT data before fitting the exponential excess. The radioimpurities in the crystal have been identified by the collaboration, with the most prominent ones given by the electron capture

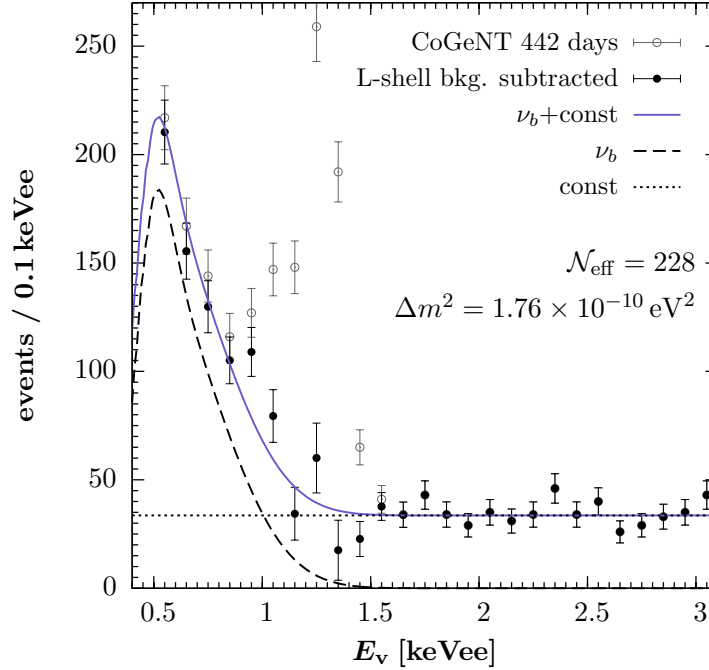


Figure 4: Recoil spectrum from the 442 live-day run of the CoGeNT experiment. The black (gray) data points show the signal after (before) subtraction of the cosmogenic radioactive background. The solid line is a fit to the black data points. It decomposes into the contribution from ν_b (dashed line) and the contribution of a constant background (dotted line.)

decays of ^{68}Ge and ^{65}Zn centered at 1.3 keVee and 1.1 keVee, respectively. From a fit of observed K-shell electron capture peaks seen in the high energy data and from the expected ratio of L-to K-shell decays one can subtract the low-energy L-shell background in the 0.5–3.2 keVee window. We follow [45] in the subtraction and collect the time-stamped events in 0.1 keVee bins. The result of this procedure can be seen in Fig. 4 as the difference between gray (with peaks) and black (peaks subtracted) data points.

Nuclear recoil energies on germanium have to be converted into the measured ionization signal. We employ a Lindhard-type, energy dependent quenching factor, $E_v(\text{keVee}) = Q \times E_R(\text{keV})^{1.1204}$ with $Q = 0.19935$ [45] and account for a finite detector resolution by convolving the recoil signal with a Gaussian of width $\sigma^2 = (69.4 \text{ eV})^2 + 0.858 \text{ eV} \times E_v(\text{eV})$ [46]. Finally, the efficiency of the detector is provided in Fig. 1 of [17].

When fitting the CoGeNT excess at low energies we follow two approaches: In the first case we seek an explanation of the excess exclusively in terms of ν_b scatterings on Ge, allowing only for a constant background contribution. In the second case we relax the assumption on the background and allow, in addition, for an exponential background component, $A \times \exp(-BE_v)$, with coefficients A and B to be determined in the fit. Clearly, in the latter approach a ν_b -induced contribution may not even be necessary as the excess resembles an exponential shape. This is therefore the most conservative way to treat the data in terms of new physics and it will show us the “compatibility” region in the $(\mathcal{N}_{\text{eff}}, \Delta m_b)$ parameter space. As mentioned above, the CoGeNT excess is likely to be revised by the collaboration. In the

second approach, the additional exponential background is here to mimic that possibility without quantifying its (yet unknown) concrete strength.

We first take the reported CoGeNT excess at face value and fit it by ν_b scatterings on Ge together with a constant background rate. The best-fit values are

$$\text{CoGeNT: } \Delta m_b^2 = 1.76 \times 10^{-10} \text{ eV}^2, \quad \mathcal{N}_{\text{eff}} = 228, \quad \chi^2/n_d = 33.6/24, \quad (27)$$

which corresponds to $p \simeq 0.1$. The background rate is $c_0 = 3.36 \text{ cpd/kg/keVee}$. A finer-grained bin size improves the goodness-of-fit to $\chi^2/n_d = 47.6/47$ with $p = 0.45$. We consider this a very good description of the data. One should keep in mind that the subtraction of the cosmogenic background has uncertainties itself which are not accounted for in the errorbar. Figure 4 shows the spectrum obtained from (27). The dashed line shows the signal from ν_b only and the solid line includes the constant background. Below $E_v \lesssim 0.5 \text{ keVee}$ the detector efficiency decreases rapidly, which explains the turn-off of the scattering signal.

Figure 6 shows the inferred 99% C.L. regions in the $(\Delta m_b^2, \mathcal{N}_{\text{eff}})$ parameter space as labeled. We use $\Delta\chi^2 = 9.21$, *i.e.* we treat the constant background rate as a nuisance parameter. This is equivalent of using a profile likelihood to infer the confidence regions. Two isolated islands are visible as labeled. The thin gray solid line labeled “CoGeNT hull” which touches the CoGeNT regions from above is obtained by allowing an additional exponential background in the fit (see discussion above.) Without further knowledge of the strength of this background, the full region below the line then becomes viable. Whenever the ν_b signal becomes too weak, the background takes over in producing a viable fit. The general expectation is that once the collaboration revises their statements about the strength of the exponential rise, the CoGeNT favored regions will move vertically downwards, but at this point it is impossible to speculate by how much. In conclusion, we find that ν_b can provide an excellent explanation to the CoGeNT data.

3.3 CRESST-II

The CRESST-II experiment [47], situated at LNGS, has recently presented their results from their DM “run32” with a total of 730 kg×days effective exposure between 2009-2011 [21]. The analysis has been carried out using data collected by eight CaWO_4 crystals which measure heat and scintillation light resulting from nuclear recoils. The calorimetric phonon channel allows for a precise determination of the recoil energy with a resolution better than 1 keV. Nuclear recoils are again quenched in scintillation light. This is a virtue as it allows for a discrimination against e^- and γ induced events. Moreover, the quenching factors of Ca, W, and O differ. To a limited degree, recoils against the respective elements can therefore be distinguished.

The analysis [21] finds an intriguing accumulation of a total of 67 events in their overall acceptance region between 10–40 keV, shown by the solid line in Fig. 5. The low-energy threshold of each detector-module is determined by the overlap between e/γ - and nuclear recoil band. Allowing for a leakage of one background e/γ -event per module distributes the individual detector thresholds between 10.2–19 keV. Whereas e/γ -events are a well controllable background, the experiment suffers from a number of less well-determined sources of

spurious events. To assess how well the observed events can be explained in terms of new physics makes the modeling of such background—unfortunately—unavoidable.

In the following we briefly mention each of the known background sources and outline our treatment of them:

1. As alluded before, the thresholds of the detector modules are chosen such that a leakage of a total number of 8 e/γ -induced events into the nuclear bands are expected. We find the energy distribution of these events by digitizing and binning the corresponding line from Fig. 11 of [21].
2. Degraded α -particles from radioactive contamination in the clamping system holding the crystals can be misidentified as nuclear recoils once their energy falls below 40 keV. A sideband analysis above that energy indicates that the distribution in recoil energy is flat. This allows to estimate the number of α -events in the acceptance region for each detector module and which is provided in Tab.2 of [21]. We follow this prescription which yields a total of 9.2 events.
3. Related to the previous source, ^{210}Pb α -decays from radioactive lead on the clamps holding the crystal and with the α -particle being absorbed by non-scintillating material constitutes another source of background. The peak at 103 keV full recoil energy in ^{206}Po is clearly visible and a fit of it allows to infer the overall exponential tail distribution in the acceptance region below 40 keV. The low-energy tail is due to ^{206}Po that is slowed down in the clamps before interacting in the crystal. We estimate the radioactive lead contamination of each detector module from the number of observed events in the reference region above 40 keV. This yields a nominal background of about 17 events.
4. Finally, low-energy neutron-nucleus scatterings in the crystals is a well known source of background. These neutrons can be produced by in-situ radioactive sources as well as by cosmogenic muons in- and out-side the detector housing. Since neutrons tend to scatter more than once, some information on the overall flux can be obtained from the amount of coincident events in different detectors. Such multiple scatters also tend to wash out the initial spectral information. The authors of [21] parameterize the neutron spectrum by a simple exponential $dN_n/dE = A \times \exp(-E/E_{\text{dec}})$ where $E_{\text{dec}} = (23.54 \pm 0.92)$ keV has been obtained from a neutron calibration run with an AmBe source. The best we can do is assuming a uniform neutron flux in all detector-modules. With $A = 1$ one gets a total of about 9 events. When fitting ν_b to the data we leave A as a free parameter. We observe that A is never too large once the goodness of the fit becomes acceptable. The reason is that the ν_b -induced spectrum experiences a relatively sharp cutoff for energies in excess of ~ 25 keV. Thus, the high-energy part of the acceptance region has to be entirely explained by background for which $A = \mathcal{O}(1)$ provides the best fit. ν_b scatters mainly on oxygen and calcium, so that there is no need to further dissect the neutron background as the latter also scatters to 90% on O [21].

In [21] the various nuclear recoil bands have not been resolved. Therefore, we compute

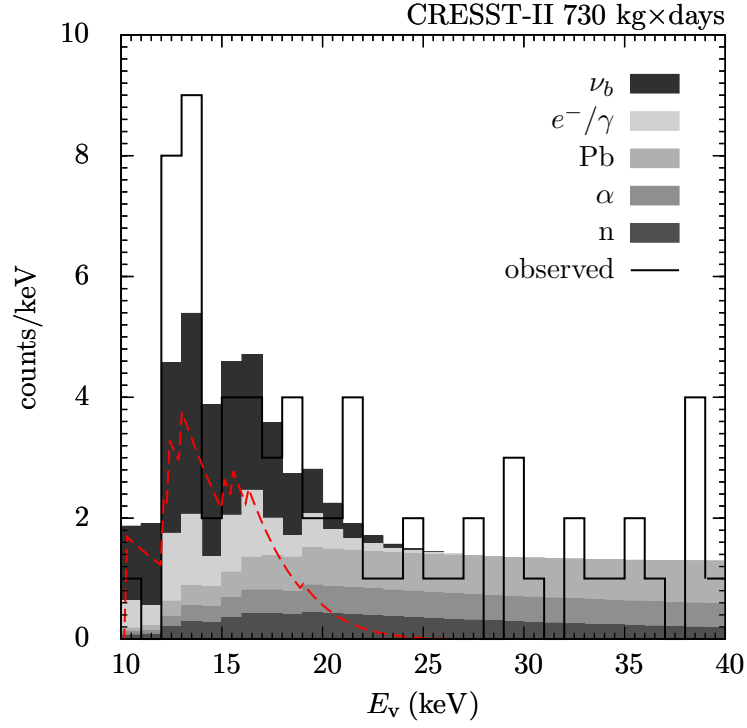


Figure 5: CRESST-II recoil spectrum. The solid line is the histogram of reported events in the 730 kg \times days run summing to a total of 67 events. The gray shaded (stacked) histograms show the best fit contribution from ν_b (darkest shading) and the modeled backgrounds as labeled and explained in the main text. The spiky dashed (red) solid line is the unbinned ν_b signal.

rate predictions for CRESST summing up all events in Ca, O, and W. The fractional exposures of the individual detector modules lie within $\sim 20\%$ of a uniform one with value $1/8$. We use the accurate values as provided by [48]. We account for a finite Gaussian energy resolution in the phonon channel with $\sigma = 1$ keV. Since the number of observed events n_i in each of the bins is small, we fit the data by minimizing the Poisson log-likelihood ratio

$$\chi_P^2 = 2 \sum_i \left[y_i - n_i + n_i \ln \left(\frac{n_i}{y_i} \right) \right], \quad (28)$$

where the sum runs over all bins and y_i is the sum of background and signal contributions; the last term is absent when $n_i = 0$. Confidence regions are directly constructed from (28).

Figure 5 shows the recoil spectrum induced by ν_b as the (magenta) continuous and falling line. Summing all background contributions to the ν_b signal the best fit parameters read,

$$\text{CRESST-II: } \Delta m_b^2 = 3 \times 10^{-10} \text{ eV}^2, \quad \mathcal{N}_{\text{eff}} = 49, \quad \chi^2/n_d = 27.7/27, \quad (29)$$

with a p -value $p = 0.48$ under the approximation that χ_P^2 in (28) follows a χ^2 distribution with $n_d = 27$. The amplitude of the neutron background is found to be $A = 1.23$. Fixing instead $A = 1$ yields the same parameters (29) with negligible degradation in χ^2 . Discontinuous jumps in the count rate when going from lower to higher recoil energies are due to the onsets of the various detector modules with increasing energy thresholds. Also shown as a stacked histogram are the modeled sources of background as labeled.

Figure 6 shows again the 99% confidence regions in the $(\Delta m_b^2, \mathcal{N}_{\text{eff}})$ parameter space. As can be seen, the favored region stretches across the plane and the trend for larger values of Δm_b^2 not shown in the plot can be easily be extrapolated. The CRESST region is compatible with the one inferred from the DAMA modulation amplitude. Once the CoGeNT excess is revised (see previous section), it is very likely that the resulting best fit region will overlap with CRESST too. CRESST spans a rather wide region in parameter space. The light yield distribution of the candidate events as a function of E_ν is not published and has thus not been accounted for. With eventual better knowledge of this quantity, the region is expected to shrink in a joint fit. In the ν_b scenario, most of the scatters are on oxygen which in turn yields most scintillation light among the CaWO_4 constituents.

It is also likely that the new CRESST data constrains larger values of \mathcal{N}_{eff} . This is especially true given that the detector model with lowest threshold only observed one count between 10–12 keV. In order to put a constraint we use what has been termed “binned Poisson” technique in [49]: for one bin, an average number of events $\nu = \nu_s + \nu_{\text{bg}}$ consisting of ν_s signal and ν_{bg} background events is excluded at a level $1 - \alpha_{\text{bin}}$ if the probability to see as few as n_{obs} observed events is α_{bin} . Since n_{obs} is a Poisson variable, α_{bin} is given the lower tail of the Poisson distribution, $\alpha_{\text{bin}} = \sum_{n=0}^{n_{\text{obs}}} \nu^n \exp(-\nu)/n!$. When dealing with more than one bin the level of exclusion $1 - \alpha$ is given by

$$1 - \alpha = (1 - \alpha_{\text{bin}})^{N_{\text{bin}}}, \quad (30)$$

where N_{bin} is the number of bins; α is the probability to see as few events as observed in at least one of the bins. For placing a constraint from CRESST we only use the bins from 10–25 keV as those are the ones for which ν_b can give a contribution. More conservative constraints are obtained when assuming that there is no background.

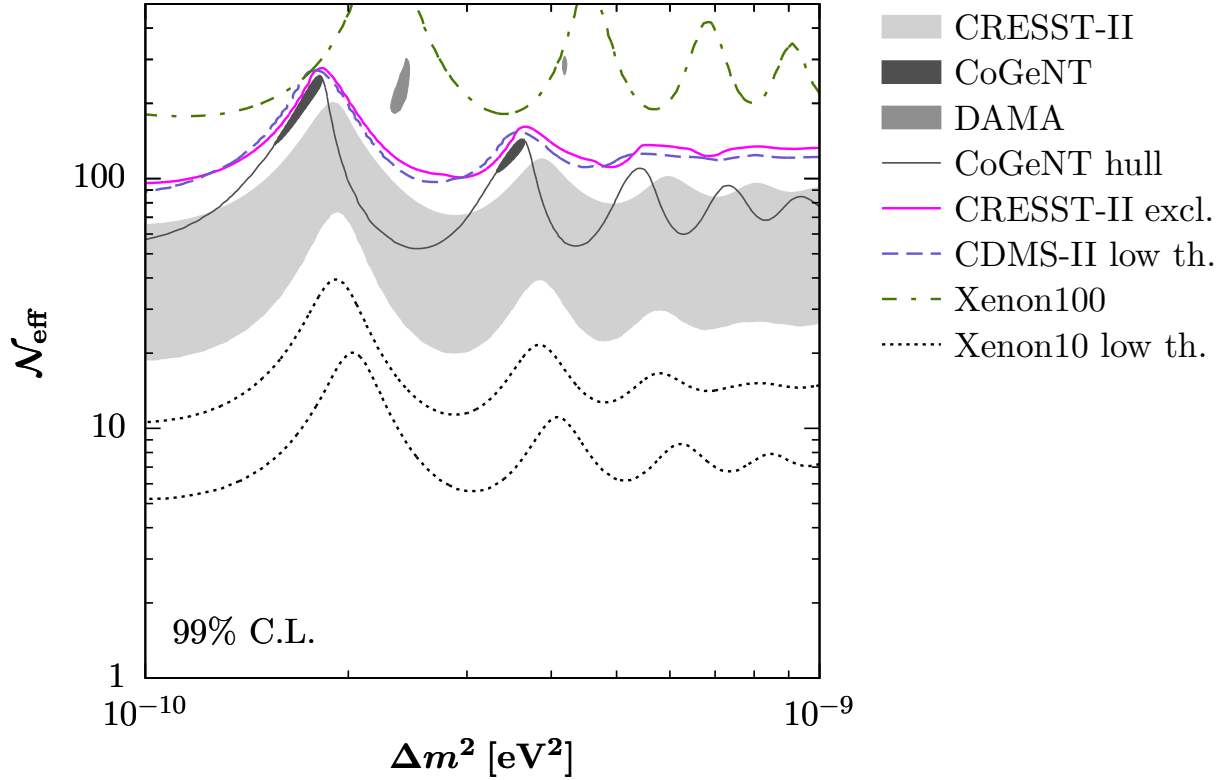


Figure 6: Summary plot of direct detection favored regions and constraints in the parameters Δm_b^2 and \mathcal{N}_{eff} at 99% confidence. *Favored regions:* the broad light shaded gray band shows the CRESST-II region. The two darkest islands are the regions in which the CoGeNT excess is explained. In presence of an exponential background contamination (*e.g.* due to “surface events”), the region below the thin gray line labeled as “CoGeNT hull” becomes in principle viable (see main text for details.) The two medium gray shaded islands indicate the regions in which the DAMA modulation amplitude is fitted; these regions as well as any other parameter choices however exhibit a tension in timing when compared to the DAMA residuals. *Constraints:* \mathcal{N}_{eff} values above the respective lines are excluded (or seriously challenged.) The top constraint is the one from Xenon100, the two degenerate ones below are obtained with the CRESST-II data and CDMS-II low-threshold data. The two dotted lines at the bottom show the constraints arising from the Xenon10 low-threshold analysis with two different assumptions on the ionization yield Q_y (see main text for details.)

3.4 Null-searches

3.4.1 CDMS-II low threshold analysis

The CDMS-II collaboration has published a low threshold analysis from the Soudan site using eight Ge detectors with a raw exposure of 241 kg days [50]. At the expense of discriminating power of e^-/γ against nuclear recoils, a threshold of 2 keV was reached. This is an interesting analysis because it uses the same target material as CoGeNT. Indeed, for the DM case the results indicate a serious conflict between the two experiments. Therefore, it is important to check if the CoGeNT explanation is also challenged in the baryonic neutrino scenario.

An exponential-like signal rise towards threshold with a maximum event rate of ~ 1 cpd/kg/keV has been observed; see Fig. 1 in [50]. “Zero-charge” events from electron recoils near the edge of the detector are expected to yield a major contribution to the observed count rate. Given that the estimation of this background involves extrapolation and hard-to-control systematic errors, we obtain the most conservative limits on \mathcal{N}_{eff} by not subtracting this background. This follows the approach taken by the collaboration itself.¹ Only the first three data bins covering $2 \text{ keV} \leq E_R \leq 3.5 \text{ keV}$ are sensitive to ν_b scattering. On those bins we perform a “binned Poisson” exclusion, similar to the one explained in Sec. 3.3. We correct for efficiency according to Fig. 1 in [50] and use a Gaussian detector resolution of 0.2 keV. In Fig. 6 we show the resulting constraint at 99% C.L. Remarkably, CDMS-II does not challenge the CoGeNT-favored regions.

3.4.2 SIMPLE

An interesting direct detection experiment in the current context is SIMPLE [52], operated in the Low Noise Underground Laboratory in southern France. It uses a dispersion of superheated liquid droplets made of $\text{C}_{12}\text{ClF}_5$ with an total active mass of 0.2 kg. Only nuclear scattering induces phase transition which results in bubble nucleation. The fact that the experiment contains mainly light elements makes it susceptible to ν_b -scattering. Notably, fluorine with atomic number $A = 19$ has a target mass fraction of $\sim 60\%$.

We use the results from Phase I of Stage II with 14.1 kg days exposure [52]. A total of 8 events were observed with an expected neutron background of 12. We include this background in the derivation of an upper limit of \mathcal{N}_{eff} as a function of Δm_b^2 . We model bubble nucleation and heat transfer efficiency following [52] for which we use an energy threshold of 8 keV. For better overview, we did not include the constraint in Fig. 6. It is superseded by the ones from CDMS-II and CRESST-II but more constraining than Xenon100 as will be discussed next.

¹It has been speculated [51] that the CoGeNT and CDMS-II recoil spectra are indeed similar after correcting for a potential energy miscalibration. Given that the status of the CoGeNT recoil spectrum is uncertain itself, we do not follow up on that discussion in this work.

3.4.3 Xenon experiments

In this work we consider the results from the Xenon10 and its upgrade, the Xenon100 experiment at LNGS [53, 8]. Currently, the most stringent constraint for spin-inelastic scattering for DM masses in the 50 GeV ballpark is the one from the Xenon100 [8]. The experiment also provides strong limits in the light-DM mass region $\mathcal{O}(10 \text{ GeV})$. In the latter context, the low-threshold analysis [54] from Xenon10 is of particular interest.

The experiments use a prompt scintillation light signal (S1) and a delayed one from ionization (S2) to detect the nature of the recoil event. Both signals are measured in units of photo-electrons (PEs). Nuclear recoil energies are obtained from the respective signals via

$$S1 : E_R = \frac{1}{\mathcal{L}_{\text{eff}}} \frac{S1}{L_y} \frac{S_e}{S_n}, \quad S2 : E_R = \frac{S2/\zeta}{Q_y}. \quad (31)$$

Only a small fraction of the deposited recoil energy is emitted in form of scintillation light. The crucial quantity is the scintillation efficiency \mathcal{L}_{eff} which it determines the discrimination threshold of the experiment. Therefore, for Xenon100 we will mostly be interested in S1 since a low-threshold analysis has not yet been published. Conversely, for Xenon10 we focus on S2. For S1 we use the measurements of [55] with a conservative extrapolation of \mathcal{L}_{eff} to zero at 2 keV nuclear recoil. $L_y = 2.2$ (Xenon100) is the light yield in PEs/keVee obtained from γ -calibration. S_e and S_n are quenching factors for scintillation light due to electron and nuclear recoils, respectively. They are experiment-specific and depend on the applied drift voltage; $S_e = 0.58$ and $S_n = 0.95$ for Xenon100. Q_y is the ionization yield per keV nuclear recoil and ζ is the measured number of PEs produced per ionized electron, $\zeta = 20$ (24) PEs for Xenon100 (Xenon10); we will comment further on Q_y below.

The S1 detector acceptance for Xenon100 is found from the lines presented in Fig. 2 of [8] together with a low-energy threshold of 4 PE which corresponds to 8.4 keV nuclear recoil energy. For S2, the trigger efficiency is effectively 100% in both experiments. We take the Poissonian nature on the expected number of scintillation photons/ionization electrons into account. For example, for S2 one computes

$$\frac{dR}{dn_e} = \int_{E_{\text{min}}} dE_R \frac{dR}{dE_R} \times \text{Pois}(n_e | \nu_e(E_R)), \quad (32)$$

where $n_e = E_R Q_y$ is the number of ionized electrons; a PMT resolution of 0.5 PE can be neglected when converting n_e to S2; $S2 = n_e \zeta$. We use a hard cut off at $E_{\text{min}} = 1.4 \text{ keV}$ following [54].

We first discuss the constraint from Xenon100. Reference [8] presents the results from a 100 day run with a fiducial detector mass of 48 kg. Three events were observed in the acceptance region 8.4–44.6 keV. We use Yellin’s maximum gap method [56] to set an upper limit. The resulting constraint is again shown in Fig. 6. Given that Xe is a rather heavy target and that the scintillation threshold is $\mathcal{O}(10 \text{ keV})$, the constraint on the parameter space is very weak. Indeed, none of the favored regions is challenged.

In contrast, a more stringent limit can be expected from the Xenon10 low-threshold analysis in [54]. Discarding the scintillation signal allows one to lower the threshold to $E_R =$

$\mathcal{O}(1 \text{ keV})$. After all cuts are applied and with a resulting effective exposure of $\sim 6.15 \text{ kg days}$ a mere number of seven events in the region $1.4 \text{ keV} \lesssim E_R \lesssim 10 \text{ keV}$ are observed. The calibration of the nuclear energy recoil scale now solely depends on Q_y [see Eq. (31)]. The problem in the analysis is that one requires Q_y in a regime where no data is available and the extrapolation of that quantity is not well supported by theoretical expectations. Indeed, the adopted values in [54] by the Xenon10 collaboration have been repeatedly disputed [57, 58]. Therefore, we adopt two different extrapolations of Q_y . First we use the solid line in Fig. 2 of [54] and second we employ more conservative choice discussed in [58] in the estimation of the energy scale.

The resulting constraints are again presented in Fig. 6. In contrast to all other null searches, Xenon10 severely challenges the entire region of interest with $\mathcal{N}_{\text{eff}} \gtrsim 20$. We caution the reader that it is also the constraint with the largest uncertainty. We will further illustrate the strong sensitivity of the results on Q_y below when considering a prospective Xenon100 low-threshold analysis.

3.5 Future sensitivity in Direct Detection

3.5.1 Xenon100 low threshold

In the previous section we have seen that a low-threshold analysis in Xenon10 can yield very stringent constraints. Therefore, it is conceivable that the collected 100 live days of data with the Xenon100 detector may offer another sensitive test for this model. Here we present projections for a Xenon100 ionization-only (S2) study.

Once the prompt scintillation signal S1 is discarded, the goal lies in lowering the threshold in S2 as much as possible. In [8] the Xenon100 quoted software threshold is 300 PE which corresponds to 20 ionized electrons. This is a factor of five larger compared to the Xenon10 low-threshold analysis. The gain in exposure by about an order of magnitude somewhat compensates for this since the increase in detector mass does not seriously affect the extraction efficiency of ionized electrons. However, an air-leak during the run introduced unwanted Kr contamination at the $(700 \pm 100) \text{ ppt}$ level. The associated rate in the electron recoil band reads,

$$R_{\text{Kr}} < 22 \times 10^{-3} \text{ cpd/kg/keVee}, \quad (33)$$

and is expected to be homogeneously distributed over recoil energy. Clearly, a putative ν_b signal must overcome this background. We remark in passing that for future runs (33) will diminish since the ^{85}Kr concentration is being continuously reduced by cryogenic distillation.

Figure 7 shows the sensitivity to ν_b with the current dataset of 100 live days for $\Delta m_b^2 = 2.5 \times 10^{-10} \text{ eV}^2$ and $\mathcal{N}_{\text{eff}} = 100$. We present the recoil spectrum as a function of actual detected S2 in units of PE. The solid lines show the ^8B and hep neutrino spectrum as labeled. The vertical dashed line indicates the Xenon100 threshold and the horizontal one is the rate (33) from Kr contamination. As can be seen, a very large signal is possible. The dotted line is again a ^8B spectrum but this time with a calibration scale following [58]. As a consequence the signal falls entirely below the threshold. Even a small change ΔE_R in

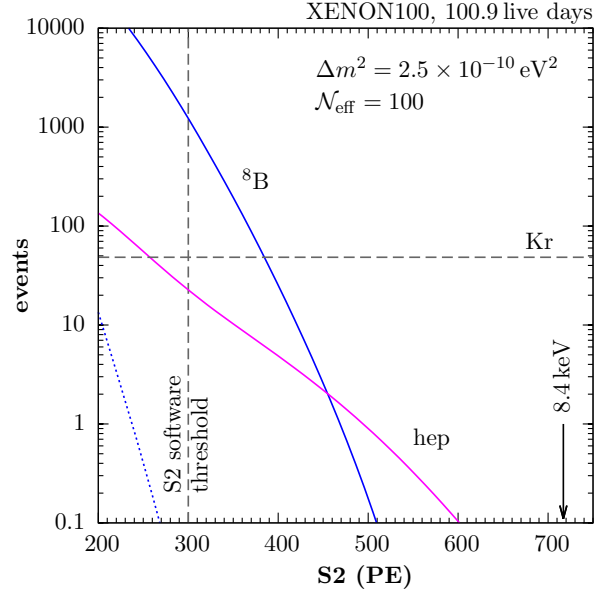


Figure 7: Projection for a Xenon100 low-threshold analysis for an exemplary parameter choice $\Delta m_b^2 = 2.5 \times 10^{-10} \text{ eV}^2$ and $\mathcal{N}_{\text{eff}} = 100$. The x -axis gives the ionization signal S2 in units of PEs. The horizontal and vertical dashed lines show the maximum rate from radioactive Kr decay and the S2 software threshold of the detector, respectively. The solid lines are the ν_b -signals from ^8B and hep neutrinos as labeled. The vertical arrow at 700 PEs indicates the current threshold of the S1 scintillation signal. The dotted line shows again ^8B neutrinos for a calibration scale following [58] instead of [54]. This highlights the severe sensitivity on the extrapolation of Q_y .

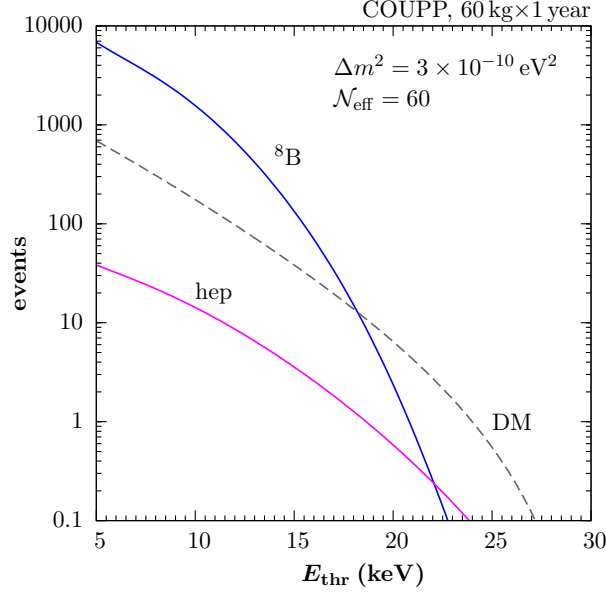


Figure 8: Predictions for a COUPP 60 kg bubble chamber for $\Delta m_b^2 = 3 \times 10^{-10} \text{ eV}^2$ and $\mathcal{N}_{\text{eff}} = 60$ as a function of bubble nucleation threshold with one year of exposure. The solid lines are from top to bottom for the ^8B and hep fluxes of ν_b . For comparison, a signal from a 10 GeV DM particle with spin-independent nucleon cross section of $\sigma_n = 10^{-41} \text{ cm}^2$ is shown.

the nuclear recoil calibration has a large effect since $\Delta S2 \sim \zeta \Delta E_R$. This illustrates 1) that the Xenon10 constraints in the previous section should be viewed with care and 2) that without further experimental insight into Q_y in (31) a conclusive prediction for Xenon100 is not feasible.

3.5.2 COUPP

As already mentioned in Sec. 3.4.2, detectors which employ fluorocarbon compounds as target material are attractive because of their favorable kinematics in contrast to heavier targets. A large scale experiment of this type is the COUPP 60 kg bubble chamber currently in the progress of moving into the SNOLAB underground facility [59]. It uses a superheated CF_3I liquid with temperature and pressure adjusted such that only nuclear recoils set off bubble nucleation events. It is a counting experiment for events above adjustable threshold without *a priori* insight into the recoil energy distribution. We assume an exposure of 1 yr together with a detector efficiency $\varepsilon = 0.7$.

Light target nuclei make COUPP particularly attractive for the searches of light WIMPs and ν_b . In Fig. 8 the integral signal of ν_b for $\Delta m_b^2 = 3 \times 10^{-10} \text{ eV}^2$ and $\mathcal{N}_{\text{eff}} = 60$ as a function of detector threshold is shown. The two solid curves from top to bottom correspond to ^8B and hep neutrinos, respectively. Already below a threshold energy of $\sim 20 \text{ keV}$ the ^8B flux induces a clear signal. Limited insight into the energy distribution should be possible by varying the rather “steplike” detector threshold. In particular, with a multi-year exposure (or larger values of \mathcal{N}_{eff}) the crossover from the ^8B to the hep neutrino spectrum may be observable. More importantly, the variation of the threshold provides discriminating power between a

putative DM signal and ν_b . The dashed line in Fig. 8 shows the integral event rate for a 10 GeV DM particle with spin-independent WIMP-nucleon cross section of $\sigma_n = 10^{-41} \text{ cm}^2$.

4 Neutrino searches

Here we are going to consider the elastic scattering of ν_b from the sun in solar neutrino experiments. The NC channels in those experiments are not necessarily sensitive to this class of new physics, given that the associated inelastic reactions exhibit the scaling (1). As shown in [12], the NCB interaction does not yield an observable rate for the D-breakup at SNO. There is also the possibility of inelastic excitation of ^{12}C with subsequent emission of a 4.44 MeV γ . The analysis of inelastic processes falls outside of the scope of the present study.

The experiments which are capable of detecting the elastic NCB signal employ hydrocarbon scintillators, namely, Borexino and KamLAND as well as the upcoming experiment SNO+. The dominant background at lowest energies comes from ^{14}C contamination of the mineral oil which decays with a maximum β energy of $Q = 156 \text{ keV}$. Other, less prominent backgrounds by long-lived isotopes at lowest energies are the β -decays of ^{85}Kr ($Q = 687 \text{ keV}$) and ^{210}Bi ($Q = 1.16 \text{ MeV}$). Unfortunately, the decays from ^{14}C prevent sensitivity to ν_b in current detectors. For example, the Borexino experiment which uses dedicated mineral oil with low residual ^{14}C content measured its concentration to be $^{14}\text{C}/^{12}\text{C} \simeq 2 \times 10^{-18}$. Though this is a seemingly small ratio, it translates into a rate of approximately $\Gamma \simeq 6 \times 10^4 \text{ events/day/ton}$ below 0.2 MeV. Therefore, in the following we restrict our analysis to a future possibility when the level of ^{14}C is much reduced so that one may hope to gain sensitivity to ν_b .

The scattering of ^8B neutrinos on protons can produce a recoil energy of $E_R \lesssim 0.5 \text{ MeV}$. However, the proton recoil is quenched and the ν_b signal may not show itself above the ^{14}C peak. In organic scintillators Birk's law provides a phenomenological description of the scintillation light yield per unit path length [60],

$$\frac{dL}{dx} = L_0 \frac{dE/dx}{1 + k_B dE/dx}, \quad (34)$$

where k_B is Birk's constant and dE/dx is the ion stopping power in the material. The formula interpolates between the limiting cases of low energy losses (no quenching), $dE/dx \ll k_B^{-1}$ with linear dependence of the light output $dL/dx \sim L_0 dE/dx$ and high energy losses (quenching), $dE/dx \gg k_B^{-1}$ for which saturation occurs, $dL/dx \sim L_0/k_B$. Equation (34) suggests the (non-linear) relation between recoil and quenched energy,

$$E_v = \int_0^{E_R} \frac{dE}{1 + k_B dE/dx}. \quad (35)$$

In the following we use Borexino, representative for other liquid scintillator experiments. It has a fiducial detector mass of 0.278 kton filled with the scintillator pseudocumene, C_9H_{12} , with a mass density of $\rho = 0.88 \text{ g/cm}^3$. We employ the SRIM computer package to obtain the stopping power dE/dx of protons in pseudocumene. Quenched energies

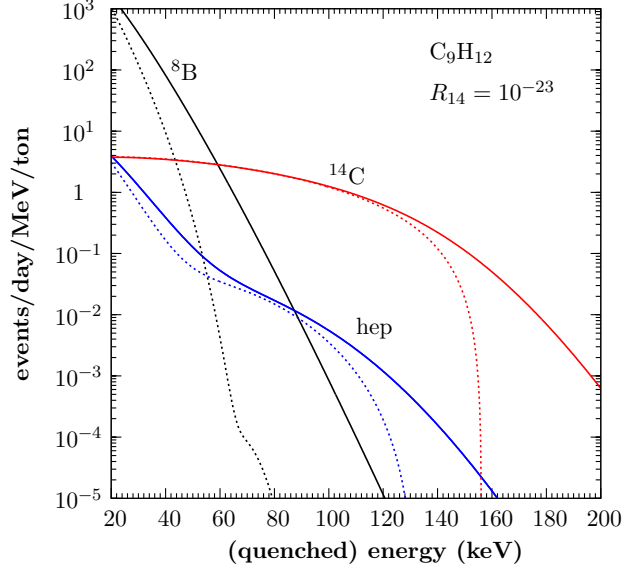


Figure 9: Liquid scintillator neutrino detector filled with pseudocumene, C_9H_{12} , and modeled after Borexino. Shown are the signals for ν_b for $\mathcal{N}_{\text{eff}} = 100$ and $\Delta m_b^2 = 2.5 \times 10^{-10} \text{ eV}^2$. The spectrum is largely dominated by background decays of ^{14}C for which a contamination in carbon of one part in 10^{-23} has been assumed. Solid (dotted) curves are with (without) detector-resolution. Proton recoil energies are quenched; the quenching of electrons at lowest recoil energies has been neglected.

are then obtained from (35) with $k_B = 0.01 \text{ cm/MeV}$. The scintillation light yield is approximately 500 PE/MeV and, for simplicity, we assume a Gaussian energy resolution with $\sigma = 0.045 \text{ MeV} \sqrt{E_v}$ [61] where E_v is in units of MeV.

We simulate the ^{14}C background spectrum as follows. The decay rate from ^{14}C decay in C_9H_{12} is given by

$$\frac{d\Gamma_{14}}{dE} = \frac{R_{14}}{t_{1/2} \ln 2} \frac{9N_A}{M_{\text{PC}}} \frac{df_{14}}{dE} = \frac{3.1 \times 10^4}{\text{day} \times \text{ton}} \left(\frac{R_{14}}{10^{-18}} \right) \times \frac{df_{14}}{dE}. \quad (36)$$

Here, R_{14} is the ratio of $^{14}\text{C}/^{12}\text{C}$, $t_{1/2} = 5730 \text{ yr}$ is the half-life of ^{14}C , N_A is Avogadro's number, and $M_{\text{PC}} = 120.2 \text{ g/mol}$ is the molecular weight of pseudocumene. The β -spectrum is given by [62],

$$\frac{df_{14}}{dE} = \frac{1}{N} \times p_e E_e (E_0 - E_e)^2 F(Z, E_e) C(E_e), \quad (37)$$

where p_e and E_e are the electron momentum and total energy, E_0 is the total endpoint energy and $F(Z, E_e)$ is the Fermi function for ^{14}N ; for the shape factor we use $C = 1 - 0.7 E_e/\text{MeV}$ [63]. N is chosen such that the spectrum is normalized to unity. Electron recoils are somewhat quenched by roughly $(10 - 40)\%$ for $(100 - 10) \text{ keV}$ [63]. For simplicity we neglect this complication here as well as more serious resolution effects near the detector threshold. In a realistic scenario, the latter can affect the spectrum below 100 keV substantially, see *e.g.* [63]. Here we are merely concerned with the question of how low the ^{14}C content needs to be in order to gain sensitivity to ν_b recoils.

In Fig. 9 we compare the ^{14}C background to a solar ν_b signal with parameters $\mathcal{N}_{\text{eff}} = 100$ and $\Delta m_b^2 = 2.5 \times 10^{-10} \text{ eV}^2$. The contamination has been fixed to $R_{14} = 10^{-23}$ which is already 5 orders of magnitude below the level for the Borexino detector, $R_{14}(\text{Borexino}) \simeq 2 \times 10^{-18}$ [64]. There is little hope that a signal would show its presence above the ^{14}C -decay endpoint energy of 156 keV. The detector resolution has the effect of smearing the cutoff out to larger values of energy, hence burying the neutrino signal. This can be seen by the difference between the dotted and solid lines. At lowest recoil energies $E_R \lesssim 60 \text{ keV}$ the ^8B signal dominates, but this may be a region which will not be explorable in large mass scintillator experiments due to their detector thresholds. Perhaps the only reasonable hope for using carbon-based scintillators is the isotopic purification of not excessively large, $O(100 \text{ kg})$, quantities of carbohydrates with the eventual setup similar to the prototype of the Borexino detector [64].

5 Conclusions

We have performed an extensive analysis of the model of ν_b neutrinos that are sourced by the sun, and elastically scatter on nuclei in underground dark matter experiments. The goal of this study was to assess the viability of this model as the explanation for the reported anomalies, that are often interpreted as a possible dark matter scattering signal. Our findings are summarized in the master plot of Figure 6, that is a direct analogue of the WIMP-mass vs. scattering cross section plot for DM scattering. We are now able to conclude the following:

- *On the positive side for the model*, the ν_b scenario with an oscillation length comparable to the earth-sun distance and with an effective enhancement of the NCB current by $O(100)$ is currently not seriously challenged by any of the existing experiments. On the contrary, this corner of parameter space provides a natural fit to the CoGeNT excess, and to the CRESST anomaly. Given enough uncertainty in the current status of the CoGeNT excess, and in the background-contaminated CRESST events, it is not difficult to see that the same regions of the parameter space of ν_b model can be responsible for these anomalies. The null results of many experiments that challenge WIMP explanations of these anomalies (such as CDMS and Xenon100), do not challenge ν_b model.
- *On the negative side for the model*, the values $\mathcal{N}_{\text{eff}} \simeq 200$ which are necessary to fit the DAMA modulation amplitude are challenged by the CDMS-II low threshold analysis and by recent CRESST-II results. It should be noted however, that in the presence of background [65], smaller values for \mathcal{N}_{eff} become viable again. This requires larger modulation amplitudes of the signal, but this can presumably be achieved. Also the phase of the predicted modulation signal is deviant from the DAMA data. Even though one can achieve a phase reversal and have a maximum in the ν_b scattering rate in early July, this is still far away from the DAMA phase, which corresponds to a modulation maximum in late May-early June. We do not know how to “correct” the model per se for this residual discrepancy. Further tension for the model may arise from a large number of events predicted for the “ionization-only” signal at Xenon10. At face value,

the parameter space of the model can potentially be constrained down to $\mathcal{N} \sim 10$, but the severity of constraint may well be mitigated by a poorly known energy calibration at those lowest recoils.

- *Future prospects* for probing ν_b -scattering look reasonably bright. In contrast to many DM models, the ν_b scattering pattern is fixed and we can make definite predictions as functions of only two parameters. For example, these predictions show that the COUPP experiment may be particularly sensitive to the ν_b scattering signal. One can also conclude that a re-designed iteration of the CRESST-II experiment with reduced backgrounds will likely be very sensitive to the ν_b model. Furthermore, a reduced electron-like background in the Xenon100 experiment will be able to probe deep into the parameter space once the uncertain values for Q_y and/or \mathcal{L}_{eff} are clarified.

Finally, as this paper was readied for the submission, a new preprint appeared [66] that examines a similar set of ideas. It expands the set of interesting mediation mechanisms beyond NCB to *e.g.* $B - L$ and “massive photon” forces with extra-light mediators in the sub-MeV mass range. Unlike the ν_b model, such modifications may already be under strong tension from astrophysical and cosmological constraints. We plan to return to ν_b -related signatures in astrophysical and cosmological settings in future work.

References

- [1] **Particle Data Group** Collaboration, K. Nakamura *et. al.*, *Review of particle physics*, *J.Phys.G* **G37** (2010) 075021.
- [2] **DAYA-BAY Collaboration** Collaboration, F. An *et. al.*, *Observation of electron-antineutrino disappearance at Daya Bay*, 1203.1669. 5 figures.
- [3] **SNO Collaboration**, Q. Ahmad *et. al.*, *Direct evidence for neutrino flavor transformation from neutral current interactions in the Sudbury Neutrino Observatory*, *Phys.Rev.Lett.* **89** (2002) 011301 [[nucl-ex/0204008](#)].
- [4] **SNO Collaboration**, B. Aharmim *et. al.*, *Combined Analysis of all Three Phases of Solar Neutrino Data from the Sudbury Neutrino Observatory*, 1109.0763.
- [5] A. Drukier and L. Stodolsky, *Principles and applications of a neutral-current detector for neutrino physics and astronomy*, *Phys. Rev. D* **30** (Dec, 1984) 2295–2309.
- [6] D. Z. Freedman, D. N. Schramm and D. L. Tubbs, *The Weak Neutral Current and Its Effects in Stellar Collapse*, *Ann.Rev.Nucl.Part.Sci.* **27** (1977) 167–207.
- [7] M. W. Goodman and E. Witten, *Detectability of certain dark-matter candidates*, *Phys. Rev. D* **31** (Jun, 1985) 3059–3063.
- [8] E. Aprile *et. al.*, *Dark Matter Results from 100 Live Days of XENON100 Data*, 1104.2549.

- [9] J. Monroe and P. Fisher, *Neutrino Backgrounds to Dark Matter Searches*, *Phys.Rev.* **D76** (2007) 033007 [0706.3019].
- [10] L. E. Strigari, *Neutrino Coherent Scattering Rates at Direct Dark Matter Detectors*, *New J.Phys.* **11** (2009) 105011 [0903.3630].
- [11] J. N. Bahcall and R. K. Ulrich, *Solar models, neutrino experiments, and helioseismology*, *Rev. Mod. Phys.* **60** (Apr, 1988) 297–372.
- [12] M. Pospelov, *Neutrino Physics with Dark Matter Experiments and the Signature of New Baryonic Neutral Currents*, 1103.3261.
- [13] R. Bernabei *et. al.*, *First results from DAMA/LIBRA and the combined results with DAMA/NaI*, *Eur. Phys. J.* **C56** (2008) 333–355 [0804.2741].
- [14] R. Bernabei *et. al.*, *New results from DAMA/LIBRA*, *Eur. Phys. J.* **C67** (2010) 39–49 [1002.1028].
- [15] A. Friedland, M. L. Graesser, I. M. Shoemaker and L. Vecchi, *Probing Nonstandard Standard Model Backgrounds with LHC Monojets*, 1111.5331.
- [16] **CoGeNT** Collaboration, C. Aalseth *et. al.*, *Results from a Search for Light-Mass Dark Matter with a P-type Point Contact Germanium Detector*, *Phys.Rev.Lett.* **106** (2011) 131301 [1002.4703].
- [17] C. Aalseth, P. Barbeau, J. Colaresi, J. Collar, J. Diaz Leon *et. al.*, *Search for an Annual Modulation in a P-type Point Contact Germanium Dark Matter Detector*, *Phys.Rev.Lett.* **107** (2011) 141301 [1106.0650].
- [18] D. Hooper and C. Kelso, *Implications of CoGeNT’s New Results For Dark Matter*, *Phys.Rev.* **D84** (2011) 083001 [1106.1066].
- [19] P. J. Fox, J. Kopp, M. Lisanti and N. Weiner, *A CoGeNT Modulation Analysis*, *Phys.Rev.* **D85** (2012) 036008 [1107.0717]. 28 pages, 14 figures, 3 tables/ version 2 has minor clarifications in the text.
- [20] J. Herrero-Garcia, T. Schwetz and J. Zupan, *On the annual modulation signal in dark matter direct detection*, 1112.1627. discussion of CoGeNT surface event subtraction added, improved statistical analysis, version to appear in JCAP, 29 pages, 9 figures, 3 appendices.
- [21] G. Angloher *et. al.*, *Results from 730 kg days of the CRESST-II Dark Matter Search*, 1109.0702.
- [22] S. Chang, J. Liu, A. Pierce, N. Weiner and I. Yavin, *CoGeNT Interpretations*, *JCAP* **1008** (2010) 018 [1004.0697].
- [23] J. L. Feng, J. Kumar, D. Marfatia and D. Sanford, *Isospin-Violating Dark Matter*, *Phys.Lett.* **B703** (2011) 124–127 [1102.4331].

- [24] J. M. Cline and A. R. Frey, *Minimal hidden sector models for CoGeNT/DAMA events*, *Phys.Rev.* **D84** (2011) 075003 [1108.1391].
- [25] T. Schwetz and J. Zupan, *Dark Matter attempts for CoGeNT and DAMA*, *JCAP* **1108** (2011) 008 [1106.6241].
- [26] M. Farina, D. Pappadopulo, A. Strumia and T. Volansky, *Can CoGeNT and DAMA Modulations Be Due to Dark Matter?*, *JCAP* **1111** (2011) 010 [1107.0715].
- [27] M. T. Frandsen, F. Kahlhoefer, J. March-Russell, C. McCabe, M. McCullough *et. al.*, *On the DAMA and CoGeNT Modulations*, *Phys.Rev.* **D84** (2011) 041301 [1105.3734].
- [28] J. Kopp, T. Schwetz and J. Zupan, *Light Dark Matter in the light of CRESST-II*, 1110.2721.
- [29] C. Kelso, D. Hooper and M. R. Buckley, *Toward A Consistent Picture For CRESST, CoGeNT and DAMA*, *Phys.Rev.* **D85** (2012) 043515 [1110.5338]. 11 pages, 7 figures.
- [30] I. M. Shoemaker and L. Vecchi, *Unitarity and Monojet Bounds on Models for DAMA, CoGeNT, and CRESST-II*, 1112.5457.
- [31] C. D. Carone and H. Murayama, *Possible light $u(1)$ gauge boson coupled to baryon number*, *Phys. Rev. Lett.* **74** (Apr, 1995) 3122–3125.
- [32] J. N. Bahcall, A. M. Serenelli and S. Basu, *New Solar Opacities, Abundances, Helioseismology, and Neutrino Fluxes*, *ApJ* **621** (Mar., 2005) L85–L88 [arXiv:astro-ph/0412440].
- [33] R. H. Helm, *Inelastic and Elastic Scattering of 187-Mev Electrons from Selected Even-Even Nuclei*, *Phys.Rev.* **104** (1956) 1466–1475.
- [34] J. N. Bahcall, E. Lisi, D. E. Alburger, L. De Braekeleer, S. J. Freedman and J. Napolitano, *Standard neutrino spectrum from ^8B decay*, *Phys. Rev. C* **54** (Jul, 1996) 411–422.
- [35] J. N. Bahcall, *Gallium solar neutrino experiments: Absorption cross sections, neutrino spectra, and predicted event rates*, *Phys. Rev. C* **56** (Dec, 1997) 3391–3409.
- [36] J. N. Bahcall, *^7Be solar neutrino line: A reflection of the central temperature distribution of the sun*, *Phys. Rev. D* **49** (Apr, 1994) 3923–3945.
- [37] **DAMA** Collaboration, R. Bernabei *et. al.*, *The DAMA/LIBRA apparatus*, *Nucl. Instrum. Meth.* **A592** (2008) 297–315 [0804.2738]. * Brief entry *.
- [38] J. P. Ralston, *One Model Explains DAMA/LIBRA, CoGENT, CDMS, and XENON*, 1006.5255.
- [39] D. Nygren, *A testable conventional hypothesis for the DAMA-LIBRA annual modulation*, 1102.0815.

- [40] K. Blum, *DAMA vs. the annually modulated muon background*, 1110.0857.
- [41] S. Chang, J. Pradler and I. Yavin, *Statistical Tests of Noise and Harmony in Dark Matter Modulation Signals*, 1111.4222.
- [42] R. Bernabei, P. Belli, F. Cappella, V. Caracciolo, R. Cerulli *et. al.*, *No role for muons in the DAMA annual modulation results*, 1202.4179.
- [43] J. Collar *UCLA Dark Matter 2012, Marina del Rey* (2012). conference talk.
- [44] B. Serfass *UCLA Dark Matter 2012, Marina del Rey* (2012). conference talk.
- [45] J. Collar. private communication.
- [46] **CoGeNT** Collaboration, C. Aalseth *et. al.*, *Experimental constraints on a dark matter origin for the DAMA annual modulation effect*, *Phys.Rev.Lett.* **101** (2008) 251301 [0807.0879].
- [47] G. Angloher, C. Bucci, P. Christ, C. Cozzini, F. von Feilitzsch *et. al.*, *Limits on WIMP dark matter using scintillating CaWO_4 cryogenic detectors with active background suppression*, *Astropart.Phys.* **23** (2005) 325–339 [astro-ph/0408006].
- [48] J. Schmalzer. private communication.
- [49] C. Savage, G. Gelmini, P. Gondolo and K. Freese, *Compatibility of DAMA/LIBRA dark matter detection with other searches*, *JCAP* **0904** (2009) 010 [0808.3607].
- [50] Z. Ahmed *et. al.*, *Results from a Low-Energy Analysis of the CDMS II Germanium Data*, 1011.2482.
- [51] J. Collar, *A comparison between the low-energy spectra from CoGeNT and CDMS*, 1103.3481.
- [52] M. Felizardo, T. Girard, T. Morlat, A. Fernandes, F. Giuliani *et. al.*, *Final Analysis and Results of the Phase II SIMPLE Dark Matter Search*, 1106.3014.
- [53] E. Aprile *et. al.*, *Design and Performance of the XENON10 Dark Matter Experiment*, *Astropart. Phys.* **34** (2011) 679–698 [1001.2834].
- [54] **XENON10** Collaboration, J. Angle *et. al.*, *A search for light dark matter in XENON10 data*, *Phys.Rev.Lett.* **107** (2011) 051301 [1104.3088].
- [55] G. Plante, E. Aprile, R. Budnik, B. Choi, K. Giboni *et. al.*, *New Measurement of the Scintillation Efficiency of Low-Energy Nuclear Recoils in Liquid Xenon*, *Phys.Rev.* **C84** (2011) 045805 [1104.2587].
- [56] S. Yellin, *Finding an upper limit in the presence of unknown background*, *Phys.Rev.* **D66** (2002) 032005 [physics/0203002].
- [57] J. Collar, *Light WIMP Searches: The Effect of the Uncertainty in Recoil Energy Scale and Quenching Factor*, 1010.5187.

- [58] J. Collar, *A Realistic Assessment of the Sensitivity of XENON10 and XENON100 to Light-Mass WIMPs*, 1106.0653.
- [59] **COUPP** Collaboration, E. Ramberg, *Developing a 60-kg bubble chamber for dark matter detection*, *Nucl.Instrum.Meth.* **A623** (2010) 454–456.
- [60] J. B. Birks, *The Theory and practice of scintillation counting*, .
- [61] B. Dasgupta and J. Beacom, *Reconstruction of supernova ν_μ , ν_τ , anti- ν_μ , and anti- ν_τ neutrino spectra at scintillator detectors*, *Phys.Rev.* **D83** (2011) 113006 [1103.2768].
- [62] M. Morita, *Beta decay and muon capture*. Addison-Wesley/WA Benjamin, Inc., Reading, MA, 1973.
- [63] H. Back, M. Balata, A. de Bari, T. Beau, A. de Bellefon *et. al.*, *Search for electron decay mode $e \rightarrow \gamma + \nu$ with prototype of Borexino detector*, *Phys.Lett.* **B525** (2002) 29–40.
- [64] **Borexino** Collaboration, G. Alimonti *et. al.*, *Measurement of the C-14 abundance in a low-background liquid scintillator*, *Phys.Lett.* **B422** (1998) 349–358.
- [65] V. Kudryavtsev, M. Robinson and N. Spooner, *The expected background spectrum in NaI dark matter detectors and the DAMA result*, *Astropart.Phys.* **33** (2010) 91–96.
- [66] R. Harnik, J. Kopp and P. A. Machado, *Exploring ν signals in dark matter detectors*, 1202.6073.